


AI-POWERED INVERSE DESIGN OF KU-BAND SIW RESONANT STRUCTURES BY ITERATIVE RESIDUAL CORRECTION NETWORK

A PREPRINT

 **Mohammad Mashayekhi**

School of Electrical Engineering
Iran University of Science and Technology (IUST)
Tehran 1684613114, Iran
masham7691@gmail.com

 **Kamran Salehian**

Department of Electrical Engineering
Amirkabir University of Technology
Tehran, Iran
k.salehian@yahoo.com

May 13, 2025

ABSTRACT

Inverse electromagnetic modeling has emerged as a powerful approach for designing complex microwave structures with high accuracy and efficiency. In this study, we propose an Iterative Residual Correction Network (IRC-Net) for the inverse design of Ku-band Substrate Integrated Waveguide (SIW) components based on multimode resonators. We use a multimode resonance structure to demonstrate that it is possible to control the resonances of the structure. Therefore, these structures can be used for resonant components and smart filter design. The proposed deep learning architecture leverages residual neural networks to overcome the limitations of traditional inverse design techniques, such as the Feedforward Inverse Model (FIM), offering improved generalization and prediction accuracy. The approach begins with a FIM to generate initial design estimates, followed by an iterative correction strategy inspired by the Hybrid Inverse-Forward Residual Refinement Network (HiFR²-Net), which we call IRC-Net. Experiments demonstrate that the IRC-Net achieves substantial improvements in prediction accuracy compared to traditional single-stage networks, validated through statistical metrics, full-wave electromagnetic simulations, and measurements. To validate the proposed framework, we first design and fabricate a three-resonance SIW structure. Next, we apply the trained IRC-Net model to predict the geometry of a four-resonance structure based on its desired frequency response. Both designs are fabricated and tested, showing strong agreement between the simulated, predicted, and measured results, confirming the effectiveness and practicality of the proposed method.

Keywords Inverse Design · Iterative Residual Correction · Deep Learning · Substrate Integrated Waveguide (SIW) · Multimode Resonators · Residual Neural Networks · Neural Networks · Inverse Electromagnetic Modeling · Smart Filter Design

1 Introduction

The Ku-band plays a pivotal role in modern communication systems, supporting critical applications such as satellite links, radar systems, and point-to-point wireless communications. Offering larger bandwidth allocations compared to lower-frequency bands, the Ku-band has become essential for contemporary telecommunication infrastructures. The rising demand for high-capacity, data-intensive applications, including HD video streaming, real-time data transmission, and broadband satellite Internet, has further intensified the need for optimized Ku-band systems, especially with the proliferation of low Earth orbit (LEO) and geostationary satellite networks [1, 2, 3].

Despite its advantages, Ku-band communication faces several challenges. Signals at higher frequencies are more prone to attenuation, interference, and environmental factors, such as rain fading, which limit the effective transmission range [4, 5]. As a result, there is a critical need for highly efficient microwave components that meet stringent performance requirements. Among these components, microwave filters play a crucial role in suppressing unwanted frequencies while

preserving the integrity of the signal. The precise design of these filters is essential to ensure effective channelization and maintain communication quality [6, 7, 8].

SIW technology has emerged as a revolutionary solution for high frequency applications, particularly in the Ku-band. By embedding rows of conductive vias into a dielectric substrate, SIW combines the advantages of conventional waveguides with the ease and cost-efficiency of planar circuit fabrication. This approach enables compact, low-loss and mass producible components, suitable for integration with antennas, amplifiers, and other microwave circuits [9, 10].

In general, designing various electromagnetic structures can sometimes be challenging. However, if one can intelligently identify the resonances of a structure and effectively control them, it becomes possible to design different functional devices, such as filters, by appropriately shaping the structures [11, 12, 13].

Traditional design approaches for electromagnetic structures, such as antenna arrays and microwave components, often rely on iterative full-wave simulations, heuristic optimization, or expert-driven trial-and-error processes. These methods, while accurate, are computationally intensive and time-consuming, particularly for high-dimensional and nonlinear design spaces. In recent years, data-driven approaches—particularly deep learning (DL)—have emerged as powerful alternatives. The DL has shown promise in both forward modeling and inverse design. Numerous studies have demonstrated the effectiveness of DL-based inverse design in a wide range of electromagnetic applications, including phase retrieval in phase antenna arrays [14], prediction of pulse widths and delays in time-modulated antenna arrays to for synthesizing of multi-beams [15], automatic metasurface synthesis over broad frequency bands [16, 17], reconfigurable terahertz antenna design [18], and electromagnetic inverse scattering [19, 20].

Building on recent advancements, researchers have increasingly applied deep learning techniques to both the forward modeling and inverse design of high-frequency microwave components. In [21], a single-stage neural network utilizing smooth ReLU and sigmoid activations is proposed for inverse modeling and parameter extraction of microwave filters. However, the model exhibits signs of overfitting, is trained on only 41 frequency samples for S-parameters, and lacks experimental validation, limiting its robustness and practical applicability.

Most research focus exclusively on either the forward or inverse problem, missing the opportunity to enforce physics consistency via a bi-directional training loop. In [22], an R-DBN-based inverse model is proposed for the first time for modeling of a sixth-order and a fourth-order multicoupled cavity filter. The learning time is relatively long, no physical implementation is reported, and only 30 S-parameter samples are used, which raises concerns about generalizability. Likewise, [23], an attention-based deep neural network combining convolutional neural network, joint channel-spatial attention, and residual connections has been proposed for forward modeling of spatio-temporal modulated (STM) non-reciprocal microwave circuits, aiming to improve prediction accuracy and generalization across various circuit configurations.

Among the limited work focused on SIW filters, [24] presents a method combining an inverse neural network with a K-impedance inverter model to synthesize a fifth-order H-plane SIW iris filter. This approach utilizes an equivalent de-embedding technique to directly extract the generalized scattering matrix, thereby avoiding conversion errors associated with equivalent rectangular waveguide models. Although results show good agreement with full-wave simulations, the method remains constrained to a fixed-order filter, is trained on a relatively small dataset, and does not accommodate a range of SIW topologies or structural variations. Furthermore, it employs conventional neural network architectures, lacking recent advances in deep learning design and training methodologies.

To address these limitations, this paper proposes a novel three-stage deep learning framework for the inverse modeling of SIW multimode resonators. The framework begins with a Feedforward Inverse Model (FIM) that generates an initial estimate of the resonator design parameters. This estimate is then refined by a Hybrid Inverse-Forward Residual Refinement Network (HiFR²-Net), which combines forward modeling with residual correction to enhance prediction accuracy. Finally, an Iterative Residual Correction Network (IRC-Net) further reduces residual errors through multiple refinement stages.

By integrating coarse-to-fine prediction, forward-consistency enforcement, and iterative residual learning, the proposed framework enables high-precision inverse design without relying on extensive electromagnetic simulations. Experimental validations confirm the method's effectiveness, demonstrating low prediction error and strong generalization performance across diverse design scenarios.

The remainder of this paper is organized as follows: Section 2 presents the design principles of substrate integrated waveguide (SIW) multimode resonator structures. A proposed configuration supporting multiple resonant modes within the Ku-band is introduced, and a comprehensive parametric study is conducted to evaluate the influence of key structural parameters on the resonance characteristics—crucial for compact and tunable filter designs. Section 3 describes the proposed deep learning framework for inverse modeling, including dataset preparation, model architecture, and training strategy. Section 4 provides a detailed analysis of the model's learning behavior, generalization performance, and

simulation-based validation. Finally, Section 5 concludes the paper with a summary of findings and suggestions for future research directions.

2 Design of Multi Mode Resonant SIW Structure

2.1 SIW Structure Overview

SIW technology has emerged as a compelling solution for high-frequency applications, particularly in the Ku-band spectrum. SIW structures emulate the characteristics of conventional rectangular waveguides while offering the advantages of planar circuit integration, such as compactness, low cost, and ease of fabrication using standard PCB processes.

SIW typically consists of a dielectric substrate sandwiched between two metal planes, with rows of metallized via holes forming the sidewalls of the waveguide. These vias confine the electromagnetic fields within the substrate, supporting the propagation of transverse electric (TE) modes.

The effective width (W_{eff}), which determines its cutoff frequency, can be approximated by:

$$W_{eff} = W - \frac{d^2}{0.95p} \quad (1)$$

where W is the width of the structure, d is the diameter of the vias, and p is the spacing between adjacent vias.

To minimize radiation losses and ensure proper wave confinement, the following design rules are typically observed:

$$p < \frac{\lambda_g}{5}, d < 2p \quad (2)$$

Here, λ_g is the guided wavelength within the SIW. Adhering to these constraints helps prevent leakage between the vias and maintains the integrity of the waveguide mode.

Multi-resonant SIW structures are realized by placing metallic posts within the SIW waveguide. These posts exhibit inductive behavior, and their proper placement enables the creation of multiple resonant frequencies. By carefully selecting the number, size, and positions of the posts, the resonances can be brought closer together, resulting in a bandpass filtering response [25, 26]. The primary degrees of freedom in the design process are the spacing between the posts, the radius of each post, and their specific locations within the structure.

Our main objective is to demonstrate the occurrence of multiple resonances and analyze how these resonances vary with different structural parameters. Therefore, we choose design parameters that yield multiple resonances at distinct frequencies. Since the posts introduce inductive loading, they are strategically placed at locations with maximum current density. Given that the field distribution in SIW structures is analogous to that of rectangular waveguides, the high-current regions can be identified with relative ease, allowing for an effective and informed post placement strategy.

In the following, we proceed to design an SIW structure incorporating the aforementioned characteristics. The design aims to achieve a multi-resonant response by exploiting the inductive nature of the posts and carefully tuning their geometrical and positional parameters. Through full-wave simulations, we analyze how variations in these parameters influence the resonant frequencies and demonstrate the potential of such structures for compact, planar filter implementations.

2.2 Physical Layout, Parameter Definition and Result of Simulation

Figure 1 illustrates the schematic of the proposed multi-resonant SIW structure, implemented on an RT5880 substrate with a thickness of 20 mils. The structure incorporates metallic vias forming the sidewalls of the waveguide, along with embedded posts distributed along the propagation path. The geometry of the structure is characterized by several critical parameters: post-to-post spacings (D_1, D_2), the radius of the coupling vias (R_1, R_2, R_3), and the offset of the posts from the sidewalls. The sidewall via diameter (d) and the via pitch (p) are fixed to ensure proper operation within the Ku-band.

The spacing between the transition line and the first post can be adjusted using the parameter G , which affects the coupling region and is defined as $G \cdot p + d$. Additional geometric parameters include the tapering width W_2 , matching width W_1 , tapering length L_2 , and matching length L_1 . The overall filter dimensions, denoted by W and L , are also indicated in the Figure 1.

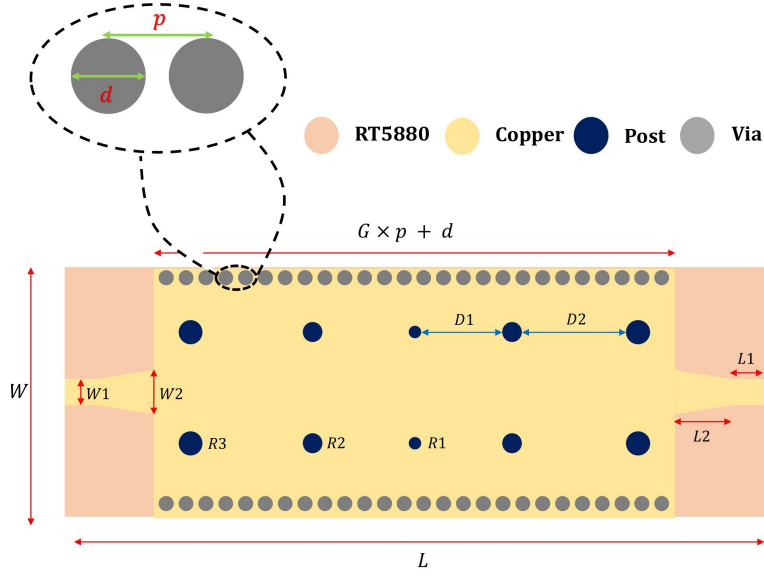


Figure 1: Schematic diagram of the multi-mode SIW structure.

As mentioned earlier, the posts act as inductive elements and should therefore be positioned at locations of maximum current within the SIW structure. It is also well established that increasing the post diameter results in higher inductance. In conventional bandpass filter design, these inductive elements are typically arranged in ascending order—i.e., from smaller to larger diameters—to achieve the desired frequency response.

However, in this study, the objective is to design a multi-mode resonator structure with widely spaced resonant frequencies, allowing us to examine how geometric variations influence the frequency shift of each individual resonance. To achieve this, the posts are deliberately arranged in descending order of diameter, from larger to smaller, to increase the separation between resonant modes.

Moreover, since the posts must be placed at the maximum current locations, their spacing is approximately set at $\lambda_g/2$. For further details and more information, see [27]. The equivalent circuit of the proposed structure, illustrated in Figure 2, uses K -inverters to represent the coupling between adjacent resonators.

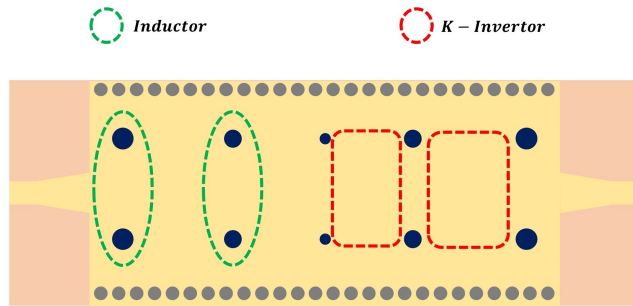


Figure 2: Equivalent circuit of the multi-mode SIW structure.

The design aims to achieve three distinct resonant frequencies within the operating band. It is also possible to obtain additional resonances within the band by increasing the number of resonators and the overall length of the structure. Additionally, multi-section structures can be employed to introduce varying impedance structures, offering greater degrees of freedom for tuning the positions of the resonant frequencies, either bringing them closer together or spacing them further apart. However, the primary objective here is to demonstrate that the proposed structure is capable of generating designer-specified resonances. The geometrical parameters for the three in-band resonances are summarized in Table 1. The values were initially selected on the basis of established design guidelines.

To evaluate the electromagnetic performance of the proposed filter, full-wave simulations were performed using CST Microwave Studio. Figure 3 presents the simulated S parameters (S_{11} and S_{21}) for the three in band resonances. The reflection coefficient (S_{11}) exhibits sharp notches at the desired center frequencies, indicating strong impedance matching. Meanwhile, the transmission coefficient (S_{21}) shows a low insertion loss throughout the passband, confirming efficient signal propagation and validating the effectiveness of the designed SIW multimode resonator.

Table 1: Geometrical parameters of the multi-mode SIW structure for three in-band resonances.

Parameter	Description	Value (mm)
W	Total width of the SIW filter structure	15
W_1	Width of the input/output taper section	1.5
W_2	Width of the internal SIW waveguide section	2
L	Length of the entire SIW filter	42.2
L_1	Length of the input taper section	1
L_2	Length of the output taper section	3
R_1	Radius of the first coupling via	0.25
R_2	Radius of the second coupling via	0.8
R_3	Radius of the third coupling via	0.9
D_1	Distance between the first and second posts	5.8
D_2	Distance between the second and third posts	8
d	Diameter of the sidewall vias forming the SIW boundary	0.8
p	Center-to-center pitch between adjacent sidewall vias	1.3
G	Scaling factor	26

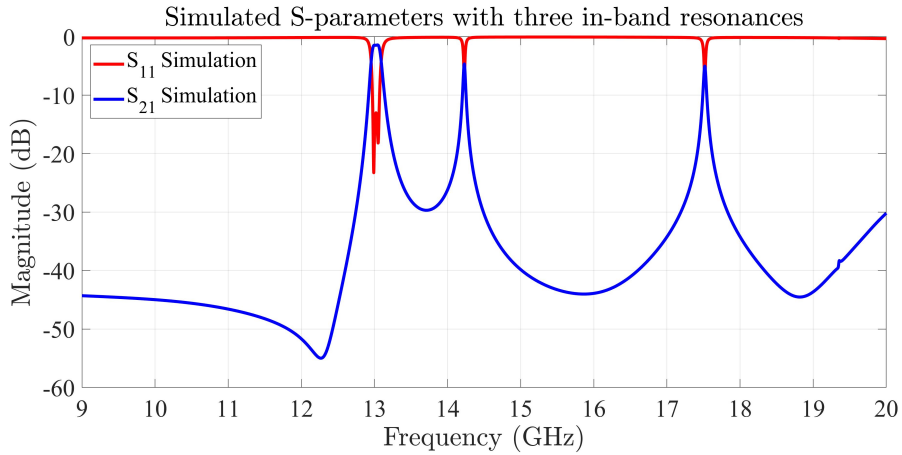


Figure 3: Simulated S parameters (S_{11} and S_{21}) of the proposed multi-mode SIW structure with 3 in-band resonances.

2.3 Investigation of the Effect of Sweeping Design Parameters

To further understand the behavior of the proposed SIW multi-mode structure, a parametric analysis was performed by sweeping critical geometrical parameters and observing their impact on the filter's electromagnetic response. Figures 4 and 5 illustrate the effect of varying the diameters D_1 and D_2 , respectively, while keeping other parameters fixed.

The sweep results show that D_1 and D_2 significantly affect the center frequencies and bandwidths of the resonant modes. For example, increasing D_1 shifts the lower resonance, causing the resonances to move closer together. On the other hand, increasing D_2 results in the resonances moving farther apart.

Given that the coupling strength changes with variations in the distances D_1 and D_2 , and consequently affects the K -inverters, it is natural and expected that these variations will influence the behavior of the S parameters.

While these sweeps offer valuable insight, they also highlight a key challenge in SIW filter design: the behavior of the structure is governed by multiple interdependent parameters. In this study, the full design is influenced not only by D_1 and D_2 , but also by R_1 , R_2 , R_3 , and G — resulting in a six-dimensional parameter space. Each parameter can affect the resonant frequencies, bandwidth, and coupling strength.

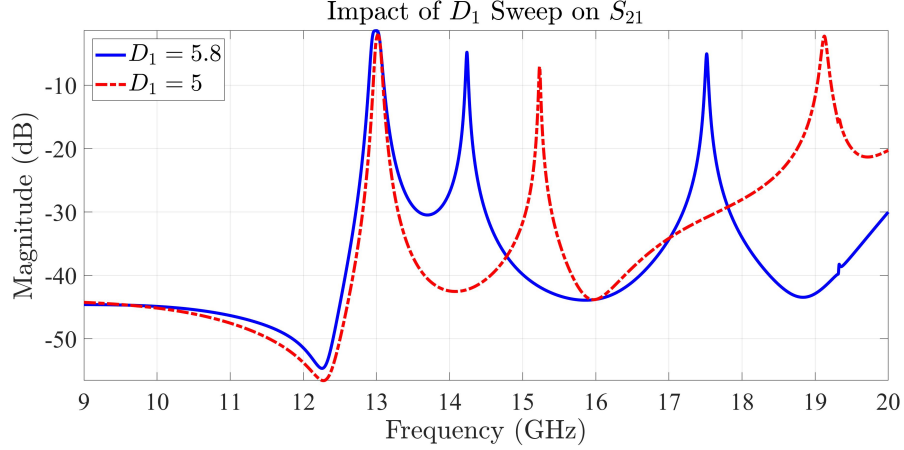


Figure 4: Effect of varying via diameter D_1 on the S parameters of the multi-mode SIW structure.

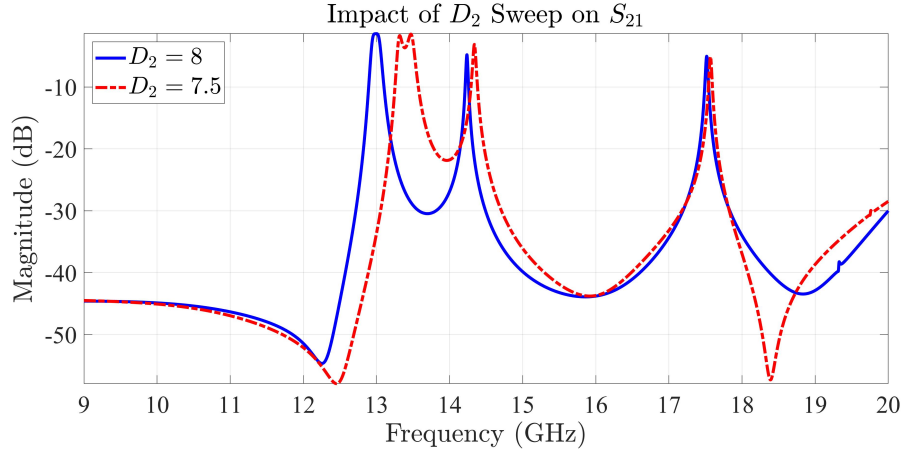


Figure 5: Effect of varying via diameter D_2 on the S parameters of the multi-mode SIW structure.

As the number of design parameters grows, performing exhaustive electromagnetic simulations becomes computationally prohibitive. Moreover, traditional design methods relying on manual tuning or iterative sweeps are inefficient and often fail to capture subtle cross-parameter interactions.

To address this complexity, we propose using deep learning to model the forward and inverse relationship between SIW geometries and their electromagnetic responses. By generating a simulation-based dataset and training a neural network, we aim to:

- Rapidly predict the design parameters for the arbitrary responses desired S_{11} and S_{21} .
- Perform inverse design, mapping desired frequency responses to optimal geometries.
- Significantly reduce the computational cost and time compared to full-wave EM simulations.

This data-driven approach is particularly suited to multi-resonant SIW structures, where multiple tightly coupled parameters must be tuned to meet stringent filter specifications. The next section details the proposed deep learning framework and dataset generation process.

3 Deep Learning Methodology

This study presents a deep learning-based framework for the inverse modeling of Ku-band SIW multimode resonators. Rather than relying on conventional single-pass or cascaded refinement strategies, the proposed approach utilizes an iterative residual correction mechanism to progressively enhance prediction accuracy through multiple feedback steps.

The overall deep learning strategy, as detailed in Section 3, is organized into four main components: dataset preparation, an initial feedforward inverse model (FIM), a hybrid inverse-forward residual refinement Network ((HiFR²-Net)), and a final iterative correction Network (IRC-Net).

3.1 Dataset Preparation

The dataset used in this study comprises **8,721 samples**, each corresponding to a unique configuration of a SIW multimode resonator. Each configuration is defined by six geometric variables: D_1 , D_2 , R_1 , R_2 , R_3 , and G , where D_1 and D_2 denote cavity dimensions, R_1 , R_2 , and R_3 represent via radius, and G is the spacing between resonators. These parameters were generated using structured nested loops, constrained by physical and electromagnetic design rules to ensure valid realizations.

To enforce physically meaningful configurations, two constraints were applied during data generation:

$$R_3 \geq R_2 \geq R_1 \quad \text{and} \quad ((R_1 + 2R_2 + D_1 + D_2 + 2R_3) \cdot 2 - 0.4) / 1.3 < G.$$

As mentioned earlier, the first constraint is used to realize the multi-mode resonator. Moreover, the second constraint ensures practical spacing between resonators and prevents overlapping via structures.

The sampling ranges were defined as follows:

- $D_1, D_2 \in [4 \text{ mm}, 10 \text{ mm}]$ with a step size of 0.5 mm,
- $R_1, R_2, R_3 \in [0.2 \text{ mm}, 1.0 \text{ mm}]$ with a step size of 0.2 mm,
- $G \in [26 \text{ mm}, 36 \text{ mm}]$.

For each valid configuration, a full-wave electromagnetic simulation was performed using CST Studio Suite to extract the S-parameter response. Specifically, the magnitude responses of S_{11} and S_{21} were sampled across the Ku-band frequency range of 12–18 GHz at 1,001 frequency points, yielding a total of 2,002 input features per sample. The average simulation time per sample was approximately three minutes on a workstation equipped with an Intel Core i7-10750H CPU and 16 GB RAM, highlighting the computational cost of conventional methods.

The dataset preparation process was structured as follows:

1. Magnitude responses of S_{11} and S_{21} were loaded from .mat files and concatenated to form the input matrix $\mathbf{X} \in \mathbb{R}^{8721 \times 2002}$.
2. Corresponding six-dimensional geometric parameters were collected and normalized, yielding the output matrix $\mathbf{Y} \in \mathbb{R}^{8721 \times 6}$.
3. All features and targets were standardized to zero mean and unit variance.
4. The dataset was randomly split into training and testing subsets with an 85%/15% ratio using a fixed seed (42) to ensure reproducibility.

This prepared dataset was used for training both the primary deep neural network model and the subsequent iterative residual correction models described in the following sections.

3.2 Feedforward Inverse Model

The Feedforward Inverse Model (FIM) serves as a traditional baseline for the inverse design problem, providing a straightforward and effective approach to estimating the geometric design parameters. This model has been widely used in various engineering fields due to its simplicity and practical utility. By leveraging a deep fully connected neural network, FIM maps high-dimensional electromagnetic scattering data directly to the corresponding low-dimensional design parameters. The key advantage of FIM lies in its ability to offer a first-order approximation of the inverse mapping, which is typically ill-posed and highly nonlinear in many real-world problems.

The primary objective of FIM is to predict the geometric design parameters \mathbf{P}_0 , which serve as an initial estimate of the true design vector \mathbf{D}_{true} . This is achieved solely based on the S-parameter data, without requiring detailed prior knowledge of the geometry. However, while effective in many cases, the simplicity of FIM can limit its performance, particularly when dealing with complex or highly nonlinear mappings. To address these challenges, FIM’s universal approximation capability, as a deep neural network, allows it to capture intricate dependencies across a wide range of SIW geometries.

The model takes as input a 2,002-dimensional vector, consisting of 1,001 frequency samples for both S_{11} and S_{21} . It is structured with seven fully connected layers that progressively decrease in size, facilitating efficient feature extraction

and compression. The ReLU activation function is employed throughout to introduce nonlinearity, while dropout regularization with a fixed rate of 10% is applied after each hidden layer to prevent overfitting. The model is trained using the mean squared error (MSE) loss function and optimized via the Adam optimizer. To prevent overtraining and ensure the model generalizes well to unseen data, early stopping is also implemented. A detailed summary of the model architecture is presented in Table 2.

This FIM provides the coarse inverse prediction \mathbf{P}_0 , which forms the basis for subsequent refinement in the overall framework. Although \mathbf{P}_0 may not precisely match \mathbf{D}_{true} , it captures the dominant structural trends required for meaningful correction. In the next stage, this estimate forms the basis for further refinement in the overall framework, which is detailed in the subsequent section, where the residual correction mechanism is introduced.

Table 2: Architecture of the Feedforward Inverse Network

Layer	Size / Type	Activation	Description
Input	2002 (Dense)	ReLU	Concatenated S-parameter vector
Hidden 1	1500 (Dense)	ReLU	Initial fully connected layer
Hidden 2	1000 (Dense)	ReLU	Intermediate layer
Dropout 1	10%	–	Regularization layer
Hidden 3	500 (Dense)	ReLU	Intermediate layer
Dropout 2	10%	–	Regularization layer
Hidden 4	250 (Dense)	ReLU	Intermediate layer
Dropout 3	10%	–	Regularization layer
Hidden 5	125 (Dense)	ReLU	Intermediate layer
Dropout 4	10%	–	Regularization layer
Hidden 6	64 (Dense)	ReLU	Intermediate layer
Dropout 5	10%	–	Regularization layer
Hidden 7	32 (Dense)	ReLU	Final hidden layer
Output	6 (Dense)	ReLU	Estimated design parameters \mathbf{P}_0

3.3 Hybrid Inverse-Forward Residual Refinement Network

Although the FIM offers a straightforward and computationally efficient approach for estimating geometric parameters from S parameters, its simplicity may hinder accurate modeling of complex inverse dynamics, particularly in ill-posed or highly nonlinear scenarios.

To enhance the prediction accuracy and consistency of inverse modeling, we introduce the Hybrid Inverse-Forward Residual Refinement Network (HiFR²-Net), schematically depicted in Figure 6. This cascaded learning framework integrates both inverse and forward learning stages, along with a residual refinement mechanism, to iteratively improve the fidelity of the design parameter estimation.

The HiFR²-Net consists of the following three stages:

- **Stage 1 – Feedforward Inverse Model (FIM):** As previously detailed, the FIM serves as a baseline inverse predictor that generates an initial estimate \mathbf{P}_0 of the normalized geometric design parameters from the input S parameters.
- **Stage 2 – Feedforward Forward Model (FFM):** The initial prediction \mathbf{P}_0 is fed into a forward model trained to reconstruct the original S-parameter vector $\hat{\mathbf{S}}$. This stage enforces forward consistency and enables indirect validation of the initial estimate through reconstruction error.
- **Stage 3 – Residual Refinement Model (RRM):** The residual vector, computed as the difference between the true and reconstructed S parameters ($\mathbf{S}_{\text{true}} - \hat{\mathbf{S}}$), is used as input to a refinement model. This model predicts a correction term $\Delta\mathbf{P}$, which is added to the initial estimate \mathbf{P}_0 to improve alignment with the true design parameters.

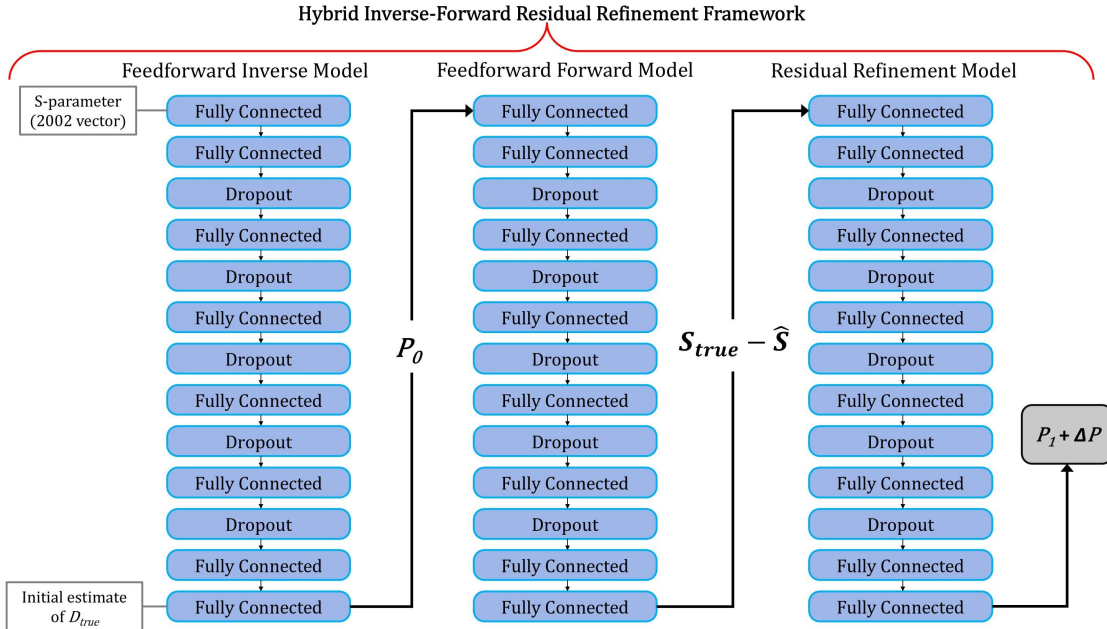
The architecture of the FFM is summarized in Table 3. It consists of multiple fully connected layers that progressively expand the input representation to reconstruct the high-dimensional S-parameter vector.

The RRM is identical to that of the FIM presented in Table 2, with the exception of its input and output: the RRM takes residual S parameters ($\mathbf{S}_{\text{true}} - \hat{\mathbf{S}}$) as input and predicts a correction to be added to the original parameter estimate ($\Delta\mathbf{P}$).

The integration of forward reconstruction and residual learning enables the system to better capture hidden dependencies and correct systematic estimation errors. In the next subsection, we further extend this idea by introducing an iterative correction mechanism to refine predictions through multiple passes.

Table 3: Architecture of the Feedforward Forward Network

Layer	Size / Type	Activation	Description
Input	6 (Dense)	ReLU	Estimated design parameters \mathbf{P}_0 from FIM
Hidden 1	32 (Dense)	ReLU	Initial expansion layer
Dropout 1	10%	–	Regularization layer
Hidden 2	64 (Dense)	ReLU	Intermediate representation
Dropout 2	10%	–	Regularization layer
Hidden 3	128 (Dense)	ReLU	Intermediate representation
Dropout 3	10%	–	Regularization layer
Hidden 4	256 (Dense)	ReLU	Progressive feature expansion
Dropout 4	10%	–	Regularization layer
Hidden 5	512 (Dense)	ReLU	Deep representation
Dropout 5	10%	–	Regularization layer
Hidden 6	1024 (Dense)	ReLU	High-capacity layer
Output	2002 (Dense)	ReLU	Reconstructed S-parameter vector $\hat{\mathbf{S}}$

Figure 6: Schematic overview of the Hybrid Inverse-Forward Residual Refinement Network (HiFR²-Net).

3.4 Iterative Residual Correction Network

The iterative residual correction Network (IRC-Net) plays a central role in enhancing the accuracy of the inverse design process. While traditional deep learning-based inverse models can yield useful initial estimates, they often fall short in capturing the full complexity of the design space due to the ill-posed and nonlinear nature of the problem.

While the concept of iterative correction has been explored in other domains, its structured integration with inverse-forward consistency and residual learning in the context of SIW multimode resonators represents a tailored and effective solution for high-fidelity inverse modeling.

The core idea behind this approach is to compute and correct the residuals—i.e., the differences between the predicted parameters and the true design parameters \mathbf{D}_{true} —at each iteration. This correction process continues until the predictions converge to a more accurate representation of the true design. Importantly, each iteration uses the same fixed

baseline output \mathbf{P}_0 from the FIM, ensuring that the initial design context remains consistent throughout the iterative process. The residuals are updated iteratively, allowing the model to gradually hone in on the correct design parameters.

This approach is particularly powerful because it enables a more detailed correction of the initial prediction by focusing on smaller, residual discrepancies that may not be captured in a single forward pass through the network. Furthermore, the modular design of the residual correction network allows for a highly flexible and interpretable architecture, making it suitable for a wide range of inverse design problems in electromagnetics and beyond.

Each iteration i involves the following steps: 1. The residual between the current prediction \mathbf{P}_{i-1} and the true design parameters \mathbf{D}_{true} is computed. 2. This residual is then modeled by a residual network, which outputs a 6-dimensional correction vector $\Delta\mathbf{P}_i$. 3. The residual correction is added to the previous prediction:

$$\mathbf{P}_i = \mathbf{P}_{i-1} + \Delta\mathbf{P}_i$$

4. The updated prediction \mathbf{P}_i becomes the input for the next correction cycle, with the process repeating for a fixed number of iterations or until convergence.

This iterative process is repeated for $T = 5$ iterations, and at the end of this loop, the final refined prediction \mathbf{P}_T represents a much closer approximation to the true design parameters. The loop's iterative nature enables the model to address subtle nonlinear discrepancies in the design parameters, significantly enhancing the model's generalization and accuracy.

The architecture of the IRC-Net used in each iteration is summarized in Table 4. It is a compact feedforward network consisting of two hidden layers with LeakyReLU activations, followed by a linear output layer that produces a 6-dimensional correction vector $\Delta\mathbf{P}_i$. This correction is then added to the previous prediction \mathbf{P}_{i-1} , progressively refining the model's estimate of the true design parameters. The use of a lightweight and consistent architecture across iterations ensures both efficiency and effective residual modeling.

A schematic representation of the proposed two-stage architecture, consisting of the FIM and IRC-Net, is shown in Figure 7. This diagram visually captures the flow of information and the key iterative refinement process at the heart of the architecture.

This modular architecture offers significant flexibility and interpretability. The FIM model captures the dominant inverse mapping, while the residual loop acts as a corrective mechanism to address subtle nonlinear discrepancies, enhancing generalization and robustness in the inverse modeling of complex electromagnetic structures.

while the iterative correction loop serves as an adaptive refinement mechanism.

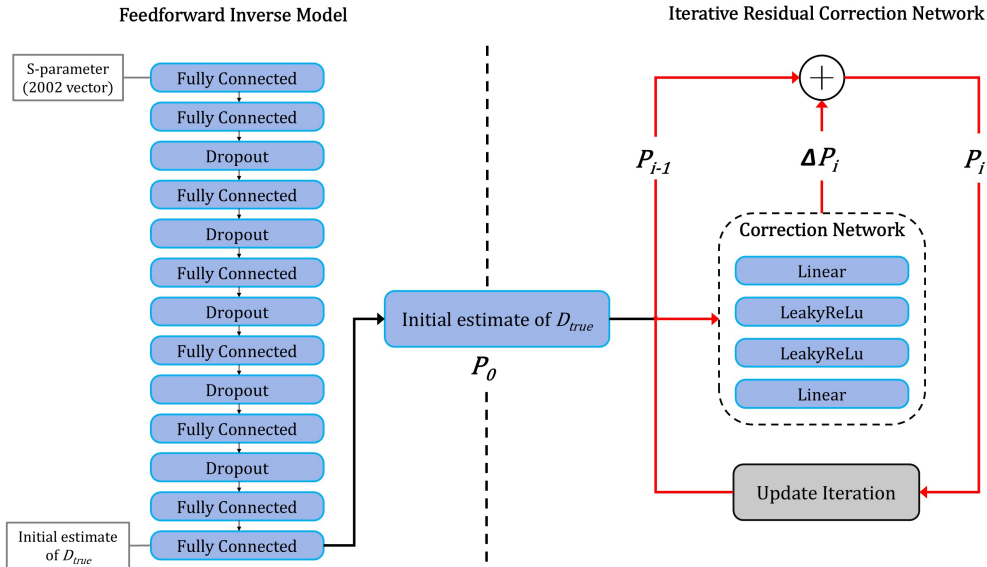


Figure 7: Schematic of the proposed two-stage architecture: a feedforward inverse model followed by iterative residual correction loops.

Table 4: Architecture of Residual Correction Network Used in Each Iteration

Layer	Size / Type	Activation	Description
Input	6 (Dense)	Linear	Fixed baseline output \mathbf{P}_0
Hidden 1	64 (Dense)	LeakyReLU	Residual mapping layer
Hidden 2	64 (Dense)	LeakyReLU	Deep residual correction
Output	6 (Dense)	Linear	Predicted correction $\Delta \mathbf{P}_i$

4 Results and Discussion

This section presents a comprehensive evaluation of the proposed deep learning framework for inverse modeling of SIW multimode resonators. The objective is to analyze the effectiveness, generalization, and practical viability of the models developed in this study. The evaluation includes both statistical assessments and full-wave simulation-based validations.

The section is organized into three main parts: (i) analysis of model learning behavior, focusing on the convergence and predictive capabilities of the FIM, the (HiFR²-Net), and the IRC-Net; (ii) statistical comparison of model performance using standard metrics; and (iii) practical validation through electromagnetic simulations and application-level implementations. This structure ensures a well-rounded assessment of both theoretical and practical aspects of the proposed methodology.

4.1 Model Learning Behavior

This subsection investigates the learning behavior of the three main components of the proposed framework: the FIM, the HiFR²-Net, and IRC-Net. The effectiveness of these models is assessed based on their ability to minimize the loss function—particularly the Mean Squared Error (MSE) and Mean Absolute Error (MAE)—during training, as well as their generalization capabilities across a set of test cases

4.1.1 Learning Behavior of the FIM

The learning performance of the FIM is assessed by examining its ability to produce an initial estimate of the design parameters, denoted as \mathbf{P}_0 . The corresponding learning curves, depicted in Figure 8, show the evolution of both training and validation errors in terms of MSE and MAE over 200 epochs.

As illustrated in the left panel of Figure 8, the MSE for both the training and validation sets rapidly decreases during the initial stages of training and continues to decline gradually until convergence. Notably, the final training and validation MSE values settle around 0.0032 and 0.0041, respectively, indicating that the model is capable of learning a reasonable initial mapping from response space to design parameters. A zoomed-in subplot highlights the stability of the learning process in the final epochs.

Similarly, the right panel presents the MAE learning curves, which follow a consistent downward trend. The training MAE reaches approximately 0.0365, while the validation MAE stabilizes around 0.0372 by the end of training. The tight gap between training and validation errors in both MSE and MAE indicates that the FIM does not suffer from overfitting and generalizes reasonably well within its single-pass prediction capacity.

Overall, the FIM demonstrates efficient and stable convergence with promising results in both training and validation phases. However, despite its effectiveness in providing an initial estimate, its performance can be further enhanced by employing an iterative refinement approach such as the Iterative Residual Correction Network (IRC-Net), which incrementally reduces prediction errors and improves model accuracy.

4.1.2 Learning Behavior of the HiFR²-Net

The learning behavior of the HiFR²-Net includes three components: the FIM, the FFM, and RRM. The learning behavior of the FIM is discussed in Section 4.1.1. This subsection focuses on the learning behavior of the FFM and RRM, as illustrated in Figure 9. The two-stage training process demonstrates how each sub-network contributes to refining the overall model performance.

In the first row of Figure 9, the learning curves of the FFM are shown. Both the MSE and MAE metrics exhibit a stair-step decline throughout training. This pattern reflects stable learning behavior, characterized by phases of rapid improvement followed by periods of stagnation, possibly due to optimization plateauing. The final training and validation MSE values converge to approximately 0.0141 and 0.0189, respectively, while the MAE values reach

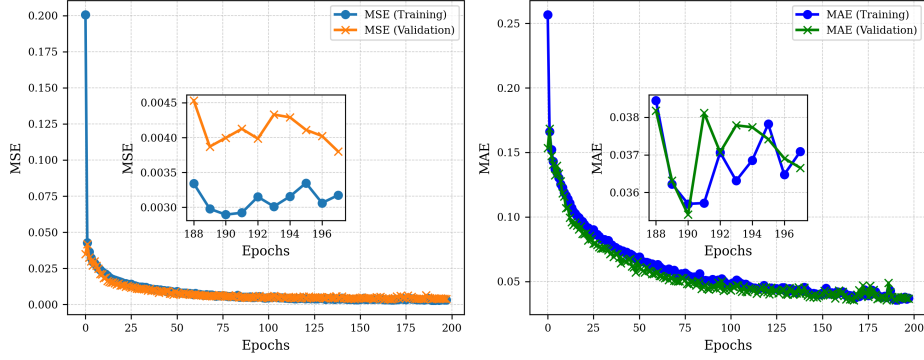


Figure 8: Learning curve for the FIM, showing the convergence of the training and validation losses.

around 0.0604 (training) and 0.0746 (validation). The small and consistent gap between training and validation metrics indicates good generalization and a reliable forward prediction baseline.

The second row of Figure 9 presents the learning curves of the RRM. The error values are very low from the beginning of training and remain nearly constant throughout the epochs. This flat curve suggests that the RRM functions primarily as a fine-tuning stage, correcting small residuals left by the FFM rather than learning from scratch. The final MSE values converge to around 0.00167 (training) and 0.00173 (validation), and the MAE values stabilize at approximately 0.0232 and 0.0247, respectively. The minimal error magnitude and narrow train-validation gap validate the RRM’s effectiveness in residual correction.

In summary, the HiFR²-Net exhibits a two-phase learning mechanism: the FFM provides an initial coarse approximation, while the RRM incrementally refines the outputs. This hierarchical correction strategy significantly enhances accuracy and generalization compared to a single-stage network.

4.1.3 Learning Behavior of the IRC-Net

Based on the output of the FIM and the refinement strategy, the IRC-Net progressively improves the prediction of design parameters through a series of residual-based updates.

Figure 10 shows the evolution of both MSE and MAE over the course of five correction iterations. The initial point in both plots corresponds to the output of the FIM, which serves as the starting prediction P_0 . As observed, the model achieves a sharp drop in error after the first iteration, with MSE reducing from approximately 0.00191 to 0.00154 and MAE dropping from approximately 0.0262 to 0.0219. Subsequent iterations continue to improve the performance, albeit with diminishing returns, eventually stabilizing with MSE around 0.00146 and MAE near 0.0209 by the fifth iteration.

Importantly, the reported error values are calculated throughout the data set, including training, validation, and test splits, ensuring a comprehensive assessment of the generalization and convergence behavior of the model.

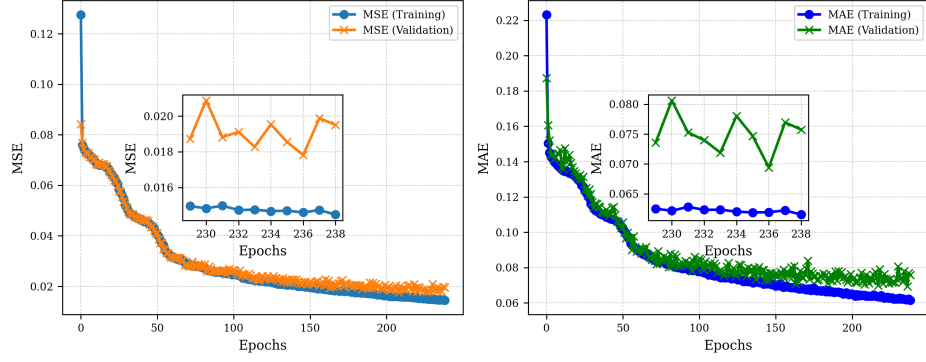
This behavior illustrates that, while the FIM provides a reasonably good initialization, the iterative correction process of IRC-Net plays a critical role in enhancing prediction accuracy. The consistent convergence trend confirms the stability and effectiveness of the residual refinement framework, making it highly suitable for tackling the challenges of complex inverse design problems.

4.2 Statistical Evaluation

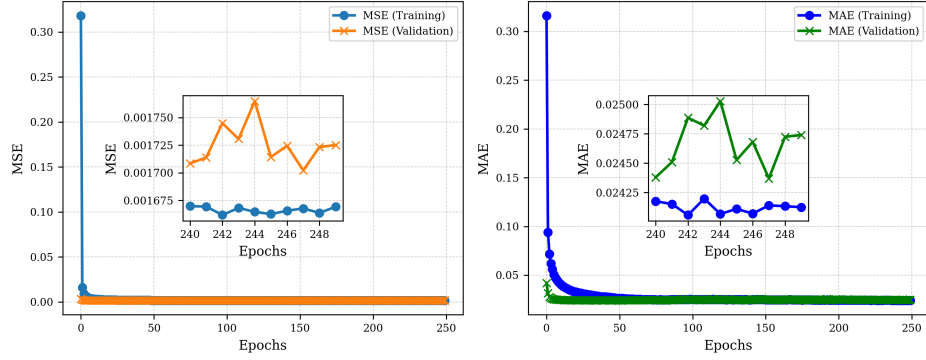
To provide a comprehensive understanding of model performance, we conducted a statistical analysis of prediction errors across the entire dataset, including training, validation, and test subsets. Two widely used error metrics, MSE and MAE, were employed to evaluate and compare the performance of the FIM, the HiFR²-Net, and the IRC-Net.

Figure 11 and Figure 12 illustrate the distribution of MAE and MSE values, respectively, on a logarithmic scale. These histograms provide insights not only into the average performance of each model but also into their consistency and robustness.

As shown in Figure 11, the MAE histogram reveals that the IRC-Net (green) achieves the lowest and most tightly clustered errors among all models. Its distribution peaks at a lower MAE value and exhibits minimal spread, indicating a high degree of consistency and fine-grained accuracy in its predictions. The HiFR²-Net (red) also demonstrates



(a) Learning curves of the FFM showing training and validation losses across epochs.



(b) Learning curves of the RRM showing training and validation losses across epochs.

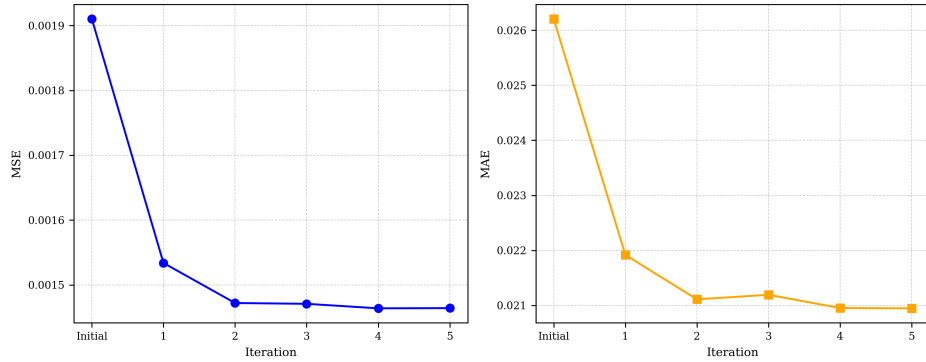
Figure 9: Training and validation loss curves for the HiFR²-Net components: (a) FFM and (b) RRM.

Figure 10: Reduction of prediction error over five iterations of the IRC-Net model. The initial point represents the output of the FIM. The errors are computed over the entire dataset (training, validation, and test).

improved performance over the baseline FIM (blue), with a shifted peak toward lower errors and a narrower spread. In contrast, the FIM shows a broader distribution with a heavier tail on the right, reflecting its relatively higher prediction variability and larger occurrence of high-error instances.

Similarly, the MSE distribution in Figure 12 supports these observations. The IRC-Net maintains a compact error distribution with the majority of its predictions concentrated around the lowest MSE values. The HiFR²-Net again performs better than the FIM by achieving a more left-shifted peak and reduced variance. Notably, the logarithmic scale highlights the IRC-Net's effectiveness in minimizing even small residual errors, a critical requirement in high-precision inverse design applications.

Collectively, the statistical evaluations and comparative visualizations confirm the superiority of the proposed IRC-Net architecture. While the FIM provides a reasonable initial estimate, it is the combination of coarse-to-fine corrections in the HiFR²-Net and the iterative residual refinement in the IRC-Net that results in highly accurate and reliable inverse design predictions. The IRC-Net’s ability to correct residual errors through multiple refinement stages proves particularly effective, enabling it to deliver more precise and robust performance across the entire dataset.

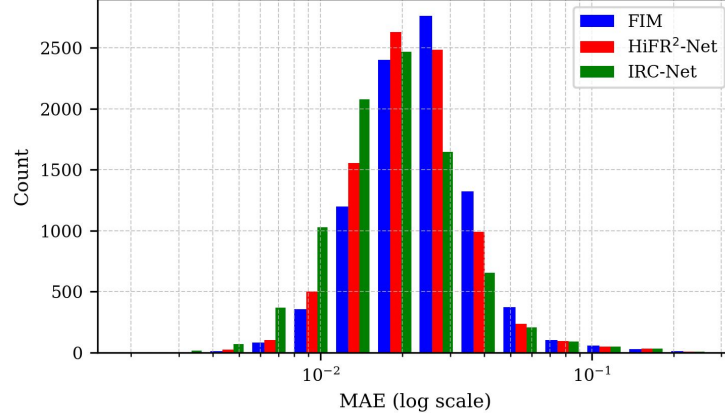


Figure 11: Histogram of MAE on a logarithmic scale for FIM, HiFR²-Net, and IRC-Net. IRC-Net achieves the lowest and most consistent MAE values.

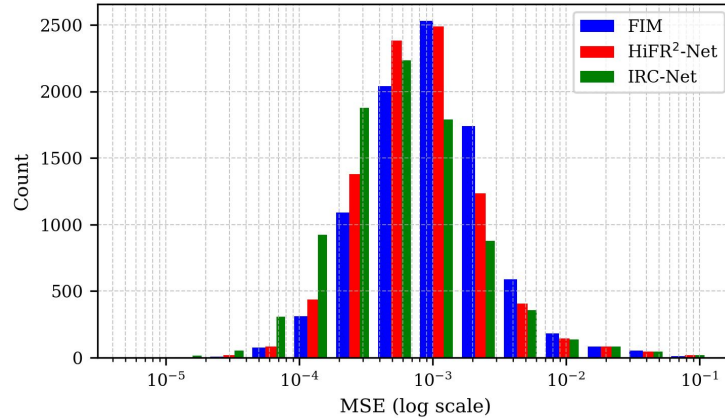


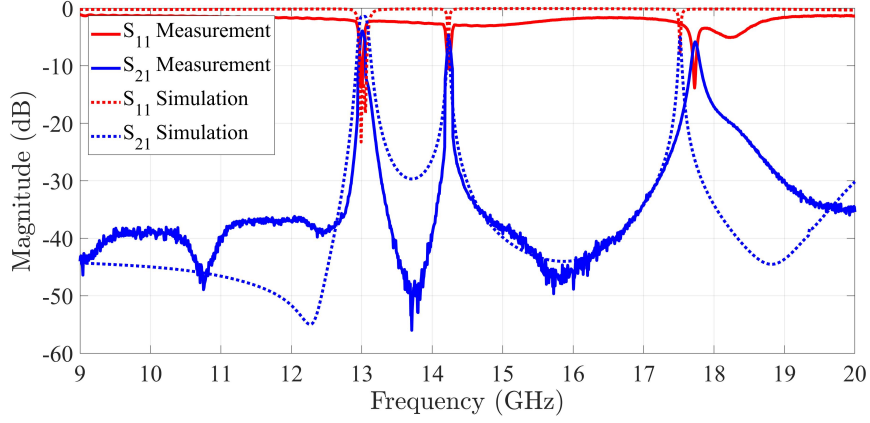
Figure 12: Histogram of Mean Squared Error MSE on a logarithmic scale for FIM, HiFR²-Net, and IRC-Net. The error distribution confirms the superior accuracy and reliability of IRC-Net.

4.3 Practical Validation through Simulation and Fabrication

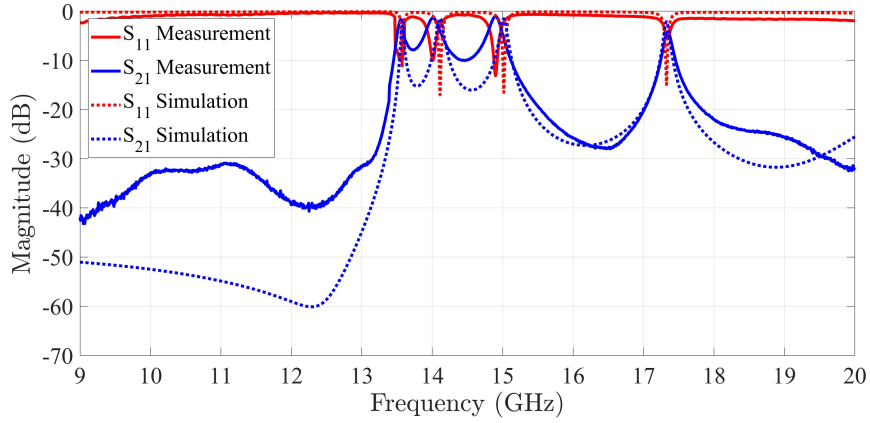
To rigorously evaluate and validate the effectiveness of the proposed inverse design framework, we conducted both simulation-based and experimental assessments. Initially, a three-resonance SIW structure was designed and manufactured using conventional full-wave electromagnetic simulations to establish a baseline for training. This structure served as the foundation for the development and fine-tuning of the IRC-Net model. Subsequently, the trained IRC-Net was employed to predict the geometric parameters of a more complex four-resonance SIW structure, based solely on its desired frequency response.

The predicted designs for both the three- and four-resonance SIW components were then evaluated through full-wave electromagnetic simulations. As illustrated in Figure 13, the simulated S parameters demonstrate a strong agreement with the target responses, confirming the model’s ability to accurately capture and replicate the desired frequency behavior across multiple resonances within the Ku-band. Figure 14 displays the measurement setup used for validation, including the fabricated SIW resonator mounted between waveguide-to-coaxial adapters.

This superior performance highlights the practical value of the proposed IRC-Net framework for robust and precise inverse electromagnetic modeling. Not only does it provide substantial improvements over single-stage architectures such as the FIM, but also ensures physical realizability, as demonstrated through successful fabrication and testing of the designed structures. These findings validate the scalability and effectiveness of the proposed method and underscore its potential for advanced RF/microwave component design in real-world applications.



(a) Structure with 3 in-band resonances.



(b) Structure with 4 in-band resonances.

Figure 13: Comparison between the measured and simulated S-parameters for the proposed multi-mode SIW structures: (a) structure with 3 in-band resonances, (b) structure with 4 in-band resonances.

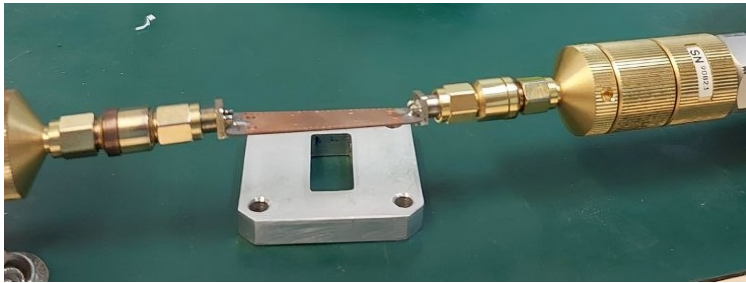


Figure 14: Measurement setup for the fabricated SIW resonator. The structure is mounted between two waveguide-to-coaxial adapters for S-parameter characterization.

5 Conclusion

In this work, we presented an efficient and accurate inverse design framework for Ku-band SIW components based on multimode resonators using a novel deep learning architecture named the IRC-Net. The proposed method integrates an initial FIM with a residual-based correction mechanism inspired by the HiFR2-Net framework, resulting in significantly enhanced prediction accuracy and generalization capabilities. Using multimode resonance structures, we demonstrated the feasibility of controlling resonance frequencies, which enables the design of complex and compact SIW-based filters and resonant components. To validate our approach, we first designed and fabricated a three-resonance SIW structure using conventional full-wave simulations, which was then used to train the IRC-Net model. The trained model was subsequently used to predict the geometric parameters of a more complex four-resonance SIW structure based solely on the desired frequency response. Both predicted structures were fabricated and tested experimentally. The measured S parameters closely matched the simulated and predicted responses, confirming the practical viability of the proposed model. Compared to traditional inverse design methods, IRC-Net significantly reduces prediction error and improves consistency across a wide range of frequency responses, as demonstrated by comprehensive statistical evaluations. This study not only introduces a new learning-based methodology for inverse electromagnetic modeling but also establishes a foundation for smart filter synthesis using data-driven techniques. The IRC-Net framework offers a scalable and generalizable solution for the inverse design of high-performance microwave components, paving the way for future research in intelligent and adaptive RF/microwave systems.

References

- [1] C.-H. Lee, A. Sutono, S. Han, K. Lim, S. Pinel, E. Tentzeris, and J. Laskar, "A compact ltcc-based ku-band transmitter module," *IEEE Transactions on Advanced Packaging*, vol. 25, no. 3, pp. 374–384, 2002.
- [2] J. Xu, W. Hong, H. Zhang, and H. Tang, "Compact bandpass filter with multiple coupling paths in limited space for ku-band application," *IEEE Microwave and Wireless Components Letters*, vol. 27, no. 3, pp. 251–253, 2017.
- [3] T. E. Humphreys, P. A. Iannucci, Z. M. Komodromos, and A. M. Graff, "Signal structure of the starlink ku-band downlink," *IEEE Transactions on Aerospace and Electronic Systems*, vol. 59, no. 5, pp. 6016–6030, 2023.
- [4] S. Scalise, H. Ernst, and G. Harles, "Measurement and modeling of the land mobile satellite channel at ku-band," *IEEE Transactions on Vehicular Technology*, vol. 57, no. 2, pp. 693–703, 2008.
- [5] R. Kennett and F. Li, "Seasat over-land scatterometer data. i. global overview of the ku-band backscatterer coefficients," *IEEE Transactions on Geoscience and Remote Sensing*, vol. 27, no. 5, pp. 592–605, 1989.
- [6] M. Qin, Z. Li, Z. Ren, P. Liu, L. Liao, X. Qiu, and Z. Li, "Varactor-based continuously tunable microstrip bandpass filters: A review, issues and future trends," *IEEE Access*, vol. 12, pp. 57 443–57 457, 2024.
- [7] P. Vryonides, S. Arain, A. Quddious, D. Psychogiou, and S. Nikolaou, "A new class of high-selectivity bandpass filters with constant bandwidth and 5:1 bandwidth tuning ratio," *IEEE Access*, vol. 12, pp. 16 489–16 497, 2024.
- [8] A. V. Zakharov and S. M. Litvintsev, "Transmission line bandpass filters with multiple attenuation poles and small number of resonators," *AEU - International Journal of Electronics and Communications*, vol. 176, p. 155131, 2024. [Online]. Available: <https://www.sciencedirect.com/science/article/pii/S1434841124000165>
- [9] A. Alam, M. S. Alam, K. Almuhan, and A. Shamim, "A critical review of interconnect options for siw technologies," *IEEE Access*, vol. 12, pp. 122 902–122 917, 2024.
- [10] J. S. Darling, V. Guruviah, and R. P. Dwivedi, "Siw technology for 5g antenna applications and beyond—a critical review," *International Journal of Communication Systems*, vol. 38, no. 2, p. e6036, 2025. [Online]. Available: <https://doi.org/10.1002/dac.6036>
- [11] S. Zarghami, S. A. Zonouri, S. Mehdipourbashi, A. Hatami, and S. M. Shah-Ebrahimi, "A high-accuracy blood glucose detection sensor using tunable bandpass filter and mlp and rbf artificial neural network algorithms," *IEEE Sensors Journal*, vol. 24, no. 6, pp. 7778–7787, 2024.
- [12] J. Uher and W. Hoefer, "Tunable microwave and millimeter-wave band-pass filters," *IEEE Transactions on Microwave Theory and Techniques*, vol. 39, no. 4, pp. 643–653, 1991.
- [13] I. Hunter and J. Rhodes, "Electronically tunable microwave bandpass filters," *IEEE Transactions on Microwave Theory and Techniques*, vol. 30, no. 9, pp. 1354–1360, 1982.
- [14] T. Iye, P. van Wyk, T. Matsumoto, Y. Susukida, S. Takaya, and Y. Fujii, "Neural network-based phase estimation for antenna array using radiation power pattern," *IEEE Antennas and Wireless Propagation Letters*, vol. 21, no. 7, pp. 1348–1352, 2022.

- [15] M. Mashayekhi and H. Soleimani, "Fundamental and harmonic beamforming of desire time-modulated planar arrays with deep learning," *IET Microwaves, Antennas & Propagation*, vol. 19, no. 1, 2025. [Online]. Available: <https://ietresearch.onlinelibrary.wiley.com/doi/abs/10.1049/mia2.70018>
- [16] F. Ghorbani, J. Shabanpour, S. Beyraghi, H. Soleimani, H. Oraizi, and M. Soleimani, "A deep learning approach for inverse design of the metasurface for dual-polarized waves," *Applied Physics A*, vol. 127, no. 11, p. 869, 2021. [Online]. Available: <https://doi.org/10.1007/s00339-021-05030-6>
- [17] F. Ghorbani, S. Beyraghi, J. Shabanpour, H. Oraizi, H. Soleimani, and M. Soleimani, "Deep neural network-based automatic metasurface design with a wide frequency range," *Scientific Reports*, vol. 11, no. 1, p. 7102, 2021. [Online]. Available: <https://doi.org/10.1038/s41598-021-86588-2>
- [18] M. Mashayekhi, P. Kabiri, A. S. Nooramin, and M. Soleimani, "A reconfigurable graphene patch antenna inverse design at terahertz frequencies," *Scientific Reports*, vol. 13, no. 1, p. 8369, 2023. [Online]. Available: <https://doi.org/10.1038/s41598-023-35036-4>
- [19] H. M. Yao, W. E. I. Sha, and L. Jiang, "Two-step enhanced deep learning approach for electromagnetic inverse scattering problems," *IEEE Antennas and Wireless Propagation Letters*, vol. 18, no. 11, pp. 2254–2258, 2019.
- [20] L. Ahmadi and A. A. Shishegar, "A physics-based deep learning to extend born approximation validity to strong scatterers," *IEEE Transactions on Antennas and Propagation*, vol. 72, no. 12, pp. 9392–9400, 2024.
- [21] J. Jin, C. Zhang, F. Feng, W. Na, J. Ma, and Q.-J. Zhang, "Deep neural network technique for high-dimensional microwave modeling and applications to parameter extraction of microwave filters," *IEEE Transactions on Microwave Theory and Techniques*, vol. 67, no. 10, pp. 4140–4155, 2019.
- [22] G. Pan, Y. Wu, M. Yu, L. Fu, and H. Li, "Inverse modeling for filters using a regularized deep neural network approach," *IEEE Microwave and Wireless Components Letters*, vol. 30, no. 5, pp. 457–460, 2020.
- [23] G. Chaudhary, Y. Meng, D. Sun Park, and Y. Jeong, "Attention-based deep neural network for high-dimensional microwave modeling of non-reciprocal bandpass filters," *IEEE Access*, vol. 13, pp. 56 220–56 236, 2025.
- [24] G.-y. Du and L. Jin, "Design of siw filter based on the equivalent de-embedding technique and inverse neural network," in *2020 IEEE 63rd International Midwest Symposium on Circuits and Systems (MWSCAS)*, 2020, pp. 407–410.
- [25] A. Adabi and M. Tayarani, "Substrate integration of dual inductive post waveguide filter," *Progress in Electromagnetics Research B*, vol. 7, pp. 321–329, 01 2008.
- [26] K. Salehian and M. Tayarani, "A novel siggw dual post band-pass filter for 5G millimeter-wave band applications with a transmission zero," *Scientific Reports*, vol. 13, no. 1, p. 20743, 2023. [Online]. Available: <https://doi.org/10.1038/s41598-023-47490-1>
- [27] N. Marcuvitz, "Waveguide handbook, peter peregrinus ltd," *London, UK*, 1986.